IET Science, Measurement & Technology

Special Section: Selected Extended Papers from the International Conference on Computational Electromagnetics (CEM) 2019

IET Journals
The Institution of Engineering and Technology

Consideration of ferromagnetic anisotropy in electrical machines built of segmented silicon steel sheets

ISSN 1751-8822
Received on 1st August 2019
Revised 10th November 2019
Accepted on 7th January 2020
E-First on 20th February 2020
doi: 10.1049/iet-smt.2019.0348
www.ietdl.org

Fabian Müller[1] ✉, Gregor Bavendiek[1], Nora Leuning[1], Benedikt Schauerte[1], Kay Hameyer[1]

[1]*Faculty of Electrical Engineering and Information Technology, Institute of Electrical Machines (IEM), RWTH Aachen University, Schinkelstraße 4, Aachen, Germany*

✉ *E-mail: fabian.mueller@iem.rwth-aachen.de*

Abstract: Electrical steel shows a distinct non-linear and anisotropic behaviour even for non-oriented steel. The flux guidance in electrical machines is realised by ferromagnetic steel sheets, and therefore it is necessary to consider the anisotropy in the simulation to have reliable and accurate results. Due to the fact that the reduction of silicon steel waste in the production process of electrical machines is crucial, and to enhance the material utilisation the segmentation is employed in the construction of electrical machines. The segmentation further allows to enhance the magnetic behaviour of the machine by considering the easy magnetisation axis in the design process. Nowadays, consideration of ferromagnetic anisotropy in the simulation of electrical machines is not accurate. To cope with these inaccuracies, in this contribution, a vectorial anisotropy model based on two-dimensional measurements is employed to the simulation of a segmented electrical machine, which is not state of the art in current machine computation. With the presented methodology, it is possible to simulate and design segmented electrical machines in an accurate fashion taking the ferromagnetic anisotropy into account.

1 Introduction

The flux guiding material in rotating electrical machines is commonly constructed of non-oriented (NO) electrical steel, which is available in many different grades that vary strongly in terms of their material characteristic and can be chosen depending on the application requirements. Even though the 'NO' in the name NO suggests more or less isotropic properties, the magnetisability varies depending on the direction of the magnetic flux along with different directions in the sheet plane. This anisotropic behaviour of NO is often neglected. It can be conjectured that this particular anisotropic phenomenon maybe one reason why simulations and measurements of losses, forces and torque are in some cases not in good accordance. For the most appropriate selection of material for an application, this direction dependence of the magnetic flux has to be considered.

In segmented machines, the magnetic anisotropy of electrical steel can be exploited to guide the flux along the easy magnetisation axis. In this case, the commonly used ideal isotropic material modulation is not sufficient to accurately describe the flux density distribution inside the geometry. Owing to the anisotropy, the magnetic resistance inside the steel laminations depends on the direction. To be able to consider this effect in the simulation of electrical machines, a vectorial anisotropic model must be employed. The measurement-based material representation (MBMR), stated in the following, is not based on an algebraic representation, and therefore it is capable of being directly used in the complicated simulations of electrical machines. Deriving the reluctivity tensor by a multi-dimensional interpolation of the magnetisation characteristic takes the angular dependency into account. The presented MBMR in combination with the finite-element method (FEM) is consecutively applied to an exemplary electrical machine built of segmented silicon steel sheets to show the influence of the ferromagnetic anisotropy.

2 Anisotropy

2.1 Basic theory

Grain-oriented (GO) electrical steel shows a very dominant magnetic anisotropy, resulting in a hard and easy magnetisation axis. For a small magnetic-field strength, the hard axis is located in the transverse direction (TD) and moves with increasing field strength toward the 55° direction due to the crystal anisotropy and sharp Goss texture of GO [1, 2]. Owing to this anisotropy and the resulting excellent properties in the rolling direction (RD), GO is mainly used for transformer applications, but it can also be employed in segmented motors as well. The strong anisotropy can, however, still be a drawback, because the flux in the segments has to divert somehow from the easy axes.

The anisotropy of NO lamination derives from the manufacturing process of the lamination and the crystal anisotropy [3–5]. In the manufacturing process, the strip is rolled and annealed, which affects the texture, i.e. the distribution of the magnetic axis, the grain size and the residual mechanical stress. In Fig. 1, the magnetisation curves for an exemplary GO material and the studied NO material are displayed, where the discussed relations are visible. The strong anisotropy and change of hard axes for GO and the still pronounced anisotropy even for NO can be observed. Owing to the favourable orientation and good magnetisation behaviour in RD, but a less pronounced anisotropy, NO can also be used for segmented motors, which will be shown in the later sections. In addition to these conventionally used materials for guiding and amplifying the magnetic flux of electrical machines, there are other interesting new materials with increased magnetic permeability that are not yet applied as an industry standard [6, 7]. However, anisotropic magnetisation behaviour has to be considered by MBMR.

The entire magnetisation process can be explained by the domain theory and is depicted in Fig. 2 [8]. In the demagnetised state, most domains are aligned randomly (Point A). Starting from a low applied field, those domains, which are oriented along the direction of the applied field, grow first by domain wall movement (Points B and C). Further increasing the applied field, domain regions, which are not aligned to the favourable direction, are occupied by properly oriented domains through wall jumps (Point D). Afterwards, the magnetic polarisation can only increase through the rotation of the magnetic momentum (Point E). Owing to the crystal anisotropy, this rotation needs more magnetic-field strength in the 45° direction than in RD or TD. Taking the anisotropy into account, results in a phase shift between the magnetic-field strength H and the magnetic flux density B.

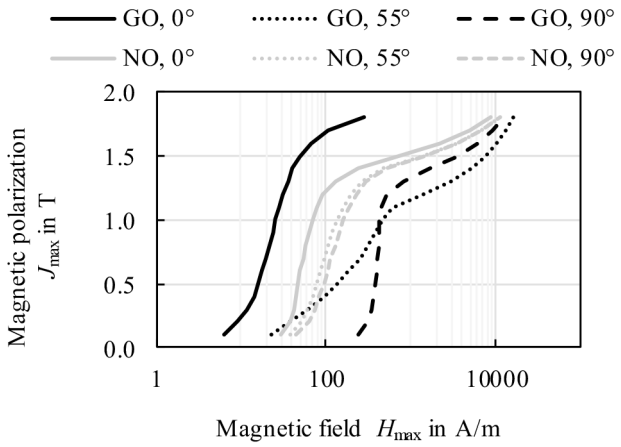

Fig. 1 *Magnetisation curves at 50 Hz for an exemplary GO and the studied NO in different angles relative to the RD*

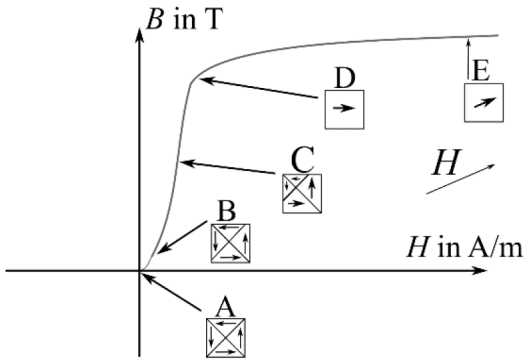

Fig. 2 *Magnetisation process of a ferromagnetic material*

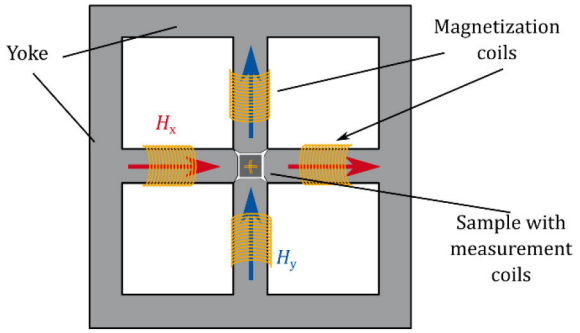

Fig. 3 *Topology of the utilised RSST*

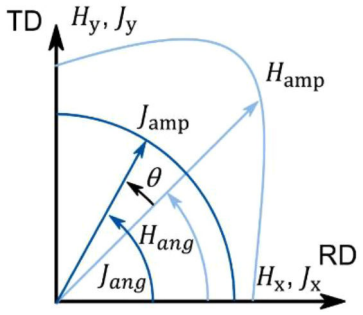

Fig. 4 *Schematic illustration of the phase shift and vectorial **B** and **H** characteristics*

2.2 Measurements

Certain measurements that aim to obtain the directional dependent behaviour can be performed in different ways such as applying unidirectional fields in different directions or rotating fields on a rotational single sheet tester (RSST) [9]. The RSST consists of a magnetic yoke and four excitation coils, each fixed on an arm of the yoke, generating the magnetic field. The sample placed in the middle of the four cross-shaped excitation yokes is equipped with two orthogonal search coils. The search coils are applied through four boring holes in the sample and enable the measurement of the vectorial flux density inside the sample.

The currents in the magnetisation coils are controlled in a way to evoke predefined spatial loci of the flux density vector inside the sample. The actual magnetic-field strength is measured by two ***H***-coils placed directly below the sample in the exactly defined distance to the sample surface.

As the ***H***-coils are positioned orthogonally, the local occurring magnetic-field strength can also be measured vectorial. This particular geometry is depicted in Fig. 3. In this paper, the measurements are performed by applying nominal flux densities from 0.1 to 1.8 T in uniaxial direction and for ten equally distributed excitation angles between 0° and 90°. This offers the opportunity to measure the vectorial characteristics of ***B*** and ***H*** with uniaxial measurements [10].

To analyse the orientation dependency of the material properly, the angle θ, illustrated in Fig. 4, must be identified in the measurements. The dependency of the anisotropy to the flux density can be directly recognised from the measurements in Fig. 5. For low flux density amplitudes, the anisotropy is comparable with an ellipse, but for high flux densities, a deviation from the ellipsoidal shape can be identified. For this reason, a simple algebraic approximation of the anisotropy such as an ellipse is not reasonable, even for NO steel sheets. In saturation, collinearity can be assumed.

The following measurements in Fig. 5 are conducted for the material M330-50A, which has a silicon content of 2.4 wt%. The measurements reveal a typical magnetic anisotropic behaviour with the highest magnetisability in the RD, a worst magnetic behaviour in the TD and the magnetic hardest behaviour in the intermediate direction between RD and TD. The angular displacement between ***H*** and ***B*** vectors is also at its maximum at this angle to the RD. This anisotropic behaviour is typical for NO electrical steels and is evaluated thoroughly in [9]. The measurement results can be used to derive a material representation including anisotropy and phase lag. The dependence on angle and amplitude needs to be fitted separately into regularised surfaces covering the magnetic anisotropy.

2.3 Measurement-based material representation

As depicted in Section 2.2, the measurements show a clear anisotropy even for NO silicon steel laminations. To incorporate this behaviour in the numerical material modelling dedicated anisotropy models have to be used. For this purpose, several models have been presented in the past, which all have their restrictions. An obvious way to start modelling anisotropy can be conducted by taking the RD and TD to create an elliptical material representation [11]. Evaluating the conducted measurements, it can be recognised that the measured data cannot be represented by an ellipsoidal model for a material saturation higher than 1.3 T. For higher flux densities, the ***H***-locus dents out in between 45° and 70° directions and the elliptical model needs to be modified [12]. Furthermore, the angular displacement between ***H*** and ***B*** is not correctly covered by an elliptical model. A next step in modelling of anisotropy by using measurement data can be found in [13, 14]. The used data of [13, 14] are unidirectionally measured in an SST and are more accurate than the ellipsoidal approach, but unfortunately, the angular information is still missing. A very accurate material representation can be found in [15, 16], which takes two-dimensional (2D) measurements to parameterise the model. To obtain an accurate model, many 2D measurements must be performed, e.g. with a uniaxial, ellipsoidal and circular forms and several inclination angles. This leads to restrictions in all models, namely accuracy of the representation for the first two models and measurement effort as well as necessary equipment for the third model.

To circumvent these limits such as the lag of angular information or the huge measurement effort, we use the opportunity to represent anisotropy directly from the measurements

into a condensed magnetisation surface [17–19]. If no RSST is available, the measurements can also be done in an SST, with the limitation of neglecting the phase lag between $\boldsymbol{H}$ and $\boldsymbol{B}$ [17]. The MBMR is based on expressing the magnetic-field strength $\boldsymbol{H}(\boldsymbol{B})$ by a linear combination of surfaces for $\boldsymbol{H}_x$ and $\boldsymbol{H}_y$. To achieve these surfaces first, the measurements depicted in Figs. 5*a* and *b* are separated into angular and amplitude information (see Fig. 6). For the measurements, the RD of the sample is placed into the *x*-direction. To make use of the crystalline symmetry, the RD has a constant angular offset of 0° and the TD of 90°. The measured data is approximated with regression splines over the amplitude and angle. Consecutively, the surfaces are refined and extrapolated by these regression splines to be dense enough to be further used as a lookup table. Alternatively, a Froehlich–Kennelly approach such as in [20] can be applied. To achieve a robust application in the FEM, the data must be at least extrapolated up to the saturation polarisation and field strength, which can be evaluated by the material composition [21]. Finally, the data points are stored in Cartesian coordinates, which need to be interpolated two-dimensionally to evaluate the material characteristics in the non-linear iteration process of the FEM.

Moreover, the reluctivity and the differential reluctivity can be directly received from the two ***H(B)*** surfaces. The reluctivity is defined as in (1). On the one side, for ideal isotropic materials, this value is a scalar, and on the other side, in not ideally isotropic materials, the reluctivity has to be evaluated in the form of a tensor as in (2). For the differential reluctivity, (3) must be evaluated

$$\nu = \frac{\boldsymbol{H}}{\boldsymbol{B}} \tag{1}$$

$$\nu = \begin{pmatrix} \frac{\boldsymbol{H}_x}{B_x} & \frac{\boldsymbol{H}_x}{B_y} \\ \frac{\boldsymbol{H}_y}{B_x} & \frac{\boldsymbol{H}_y}{B_y} \end{pmatrix} \tag{2}$$

$$\nu_{\mathrm{d}} = \begin{pmatrix} \frac{\partial \boldsymbol{H}_x}{\partial B_x} & \frac{\partial \boldsymbol{H}_x}{\partial B_y} \\ \frac{\partial \boldsymbol{H}_y}{\partial B_x} & \frac{\partial \boldsymbol{H}_y}{\partial B_y} \end{pmatrix} \tag{3}$$

The anisotropic behaviour of the measured material can be clearly depicted in Fig. 6. The angular information is shown in Fig. 6*b* and is comparable with the measured values, and for flux densities higher than 1.6 T an effect of the saturation is visible. In saturation, the angular displacement between $\boldsymbol{H}$ and $\boldsymbol{B}$ is assumed to vanish. Furthermore, it is crucial that the surfaces contain no local minima, which would lead to numerical challenges for the non-linear simulation.

3 Magnetostatic-field calculation

The magnetostatic-field problem is solved by the FEM with the magnetic vector potential. The problem region Ω is the domain with a boundary Γ holding unary and binary boundary conditions $[\Gamma = (\Gamma_u \cup \Gamma_b)]$. The domain holds subdomains Ω_{c}, in which current densities are imposed and subdomains Ω_{ani} and Ω_{iso} with anisotropic and isotropic materials. The strong formulation for the magnetic vector potential arises from Ampère's law stated in the equation below:

$$\nabla \times \boldsymbol{H} = \boldsymbol{J} \tag{4}$$

The magnetic vector potential is defined as in (5). Substitution of (5) into the Ampère's law (4) results in the magnetostatic vector potential formulation (6)

$$\nabla \times \boldsymbol{A} = \boldsymbol{B} \tag{5}$$

$$\nabla \times \boldsymbol{\nu} \nabla \times \boldsymbol{A} = \boldsymbol{J} \tag{6}$$

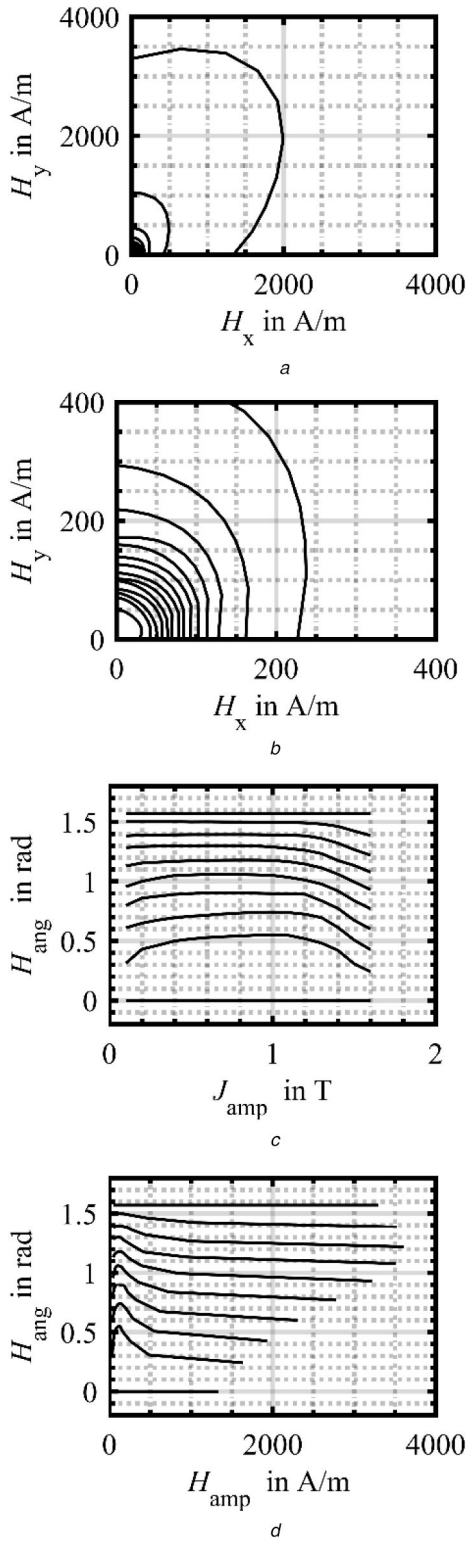

Fig. 5 *Measured magnetic-field strength excited by controlled alternating flux densities with a frequency of 50 Hz for iron–silicon (Fe–Si) 2.4%*
(a) ***H***-loci for high excitations, ***(b)*** ***H***-loci for small excitations, ***(c)*** $\boldsymbol{H}_{\mathrm{ang}}(\boldsymbol{J}_{\mathrm{amp}})$, ***(d)*** $\boldsymbol{H}_{\mathrm{ang}}(\boldsymbol{H}_{\mathrm{amp}})$

Considering the strong non-linear behaviour of the ferromagnetic material in the rotor and stator of the machine, a non-linear iteration scheme must be employed. A widely implemented and established approach is the Newton method [19, 22–25]. Starting from a first linear solving of (6), it is applied by linearising (6) in the resulting point by a first-order Taylor approximation. This linearisation is stated in the equation below:

$$\boldsymbol{P}^k \cdot \Delta \boldsymbol{A}^k = \boldsymbol{J} - (\nabla \times \boldsymbol{H}(\boldsymbol{B})) \tag{7}$$

In (7), $\boldsymbol{P}^k$ is the Jacobian matrix, which contains the derivation of the material behaviour in the current iteration and $\Delta\boldsymbol{A}^k$ is the correction of $\boldsymbol{A}$. If the material is part of Ω_{iso}, the Jacobian can be evaluated by the equation below:

$$\frac{\partial \boldsymbol{H}}{\partial \boldsymbol{B}} = \frac{\partial \nu}{\partial \boldsymbol{B}^2} 2\boldsymbol{B}^2 + \nu \tag{8}$$

Even though this is the standard approach in most finite-element (FE) solvers, it leads to a loss of directional information. Owing to this reason in anisotropic regions Ω_{ani}, the differential Newton method is utilised. The differential reluctivity (3) holds the material information for the Jacobian matrix. For evaluation of $\boldsymbol{H}(\boldsymbol{B})$, the surfaces for $\boldsymbol{H}_x$ and $\boldsymbol{H}_y$ of the MBMR are used. To receive a unique solution the Coulomb gauge, as stated in (9), must be satisfied, besides the boundary conditions. For the 2D case, the gauge condition is implicitly given in the equation below:

$$\nabla \cdot \boldsymbol{A} = \frac{\partial A_z(x, y)}{\partial z} = 0 \tag{9}$$

If the RD in the simulation should not be placed in the x-direction, a coordinate transformation must be considered. When evaluating the change of the coordinate system, two options are given: either inside the non-linear solving procedure or in the pre-processing stage. If it is to be calculated in the processing stage, the Cartesian vector has to be transformed into a new system with RD and TD as basis using (10). In this new system $\boldsymbol{H}$, ν and ν_{d} have to be evaluated, and finally transformed back into the Cartesian system with the aid of (11) and (12). Replacing ν by ν_{d} in (12) holds the back transformation for the differential reluctivity tensor

$$\boldsymbol{B}_{\text{rdtd}} = \begin{pmatrix} \cos(\alpha) & \sin(\alpha) \\ -\sin(\alpha) & \cos(\alpha) \end{pmatrix} \cdot \boldsymbol{B}_{xy} \tag{10}$$

$$\boldsymbol{H}_{xy} = \begin{pmatrix} \cos(\alpha) & -\sin(\alpha) \\ \sin(\alpha) & \cos(\alpha) \end{pmatrix} \cdot \boldsymbol{H}_{\text{rdtd}} \tag{11}$$

$$\boldsymbol{\nu}_{xy} = \begin{pmatrix} \cos(\alpha) & -\sin(\alpha) \\ \sin(\alpha) & \cos(\alpha) \end{pmatrix} \cdot \boldsymbol{\nu}_{\text{rdtd}} \cdot \begin{pmatrix} \cos(\alpha) & \sin(\alpha) \\ -\sin(\alpha) & \cos(\alpha) \end{pmatrix} \tag{12}$$

α is the angular offset of the materials RD toward the x-axis. It can be characterised that the transformations must be evaluated in every element in each iteration step, and therefore this results in extensive computational effort.

By turning the region's material surfaces in the pre-processing stage, this computation effort can be avoided. The presented method and material model are implemented in the software package iMOOSE, developed by the Institute of Electrical Machines RWTH Aachen (IEM).

4 Simulation of a segmented electrical machine

During the design process of electrical machines, many factors need to be considered. Besides global quantities such as the torque and losses, the production costs are also of interest. Therefore, it is worthwhile to decrease the material waste in the production, particularly relating to the cutting of the steel laminations [26]. Usually, if stator and rotor consist of the same material, both are punched simultaneously, as depicted in Fig. 7*a*. For improving the material utilisation, other cutting techniques can be used especially for machines with tooth windings, see Fig. 7*b*. How the segmentation is realised depends on many prerequisites. While the rotor guides unidirectional fields, which are almost constant in time, it experiences high centrifugal forces. Owing to this mechanical requirement, the segmentation of high-speed rotors such as in turbo generators is not reasonable. In general, it can be outlined that the segmentation of the rotor is limited by speed, and therefore it does not apply to the entire power range [26]. The stator partly holds areas with almost unidirectional fields, but also rotating fields appear at the transition of the teeth into the yoke. In the teeth, mostly unidirectional fields occur. The mechanical forces that the stator has to withstand originate mainly from the fitting and also from the electromagnetic force acting on the tip of the teeth. The segmentation method of the rotor is dominated by mechanical requirements, while the design of the stator segments is dominated by the magnetic-field requirements.

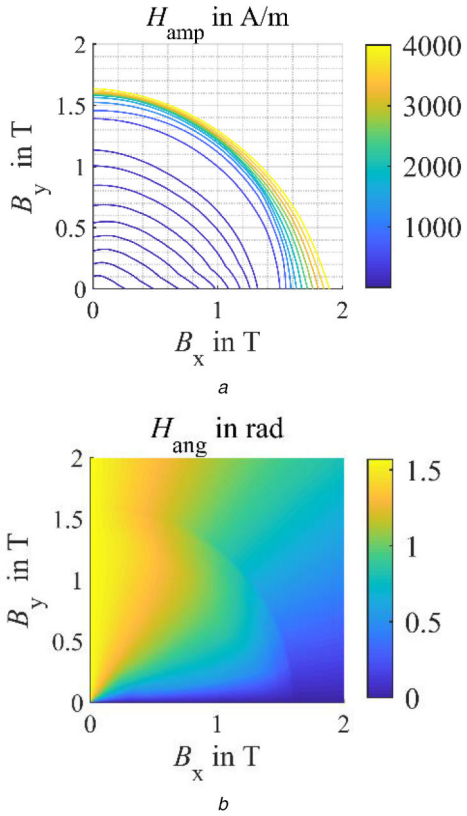

Fig. 6 *H(B) surfaces derived from RSST measurements*
(a) $\boldsymbol{H}_{\text{amp}}(B_x, B_y)$, ***(b)*** $\boldsymbol{H}_{\text{ang}}(B_x, B_y)$

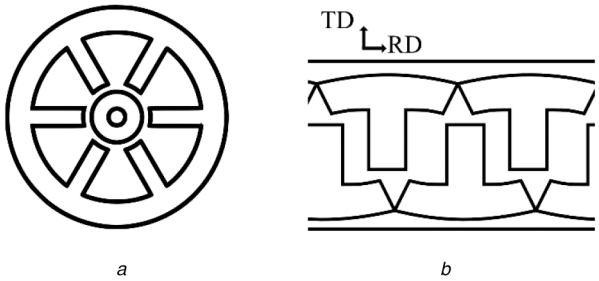

Fig. 7 *Different cutting methods for steel laminations used in electrical machines*
(a) Conventional cutting not segmented, ***(b)*** Segmented

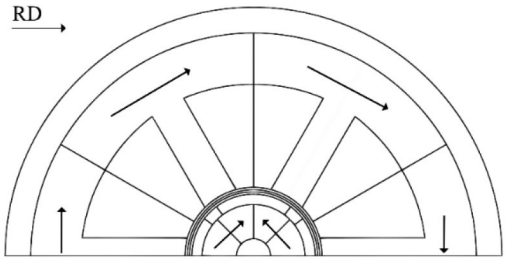

Fig. 8 *Segmented machine design; the arrows indicate the easy axis of the steel sheets/segments*

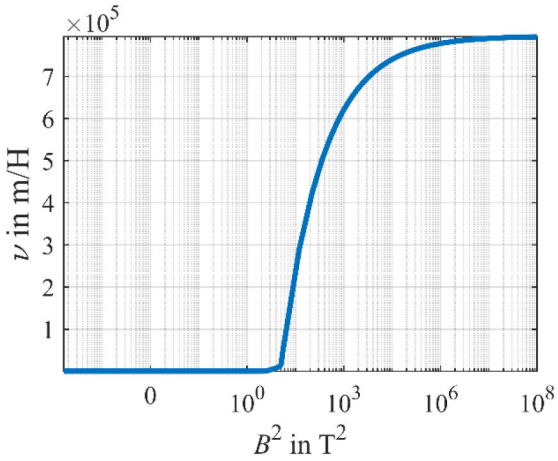

Fig. 9 *Scalar material characteristic of Fe–Si 2.4%*

On the one hand, the assembly of segmented machines needs automated processes and is more complicated due to a larger number of pieces compared with the conventional method. On the other hand, the segmented pieces lower the requirements regarding the stamping and the material consumption; thus, the material cost can be reduced significantly. Moreover, the manufacturing of the single teeth allows the coil to be wound around it, which results in 20–30% higher slot filling rates [27]. Unfortunately, the manufacturing of segmented machines can evoke parasitic effects as, for example, secondary air gaps between the segments and higher losses due to the increased number of cut edges [28]. Such secondary air gaps also lead to the necessity of applying this segmentation to machines that are not sensitive to small deviation regarding the air gap or to consider it in the stapling process. If the machine is properly constructed, the segmentation is possible for induction machines and reluctance machines as well.

For these reasons, an exemplary small-scale synchronous machine is simulated as follows. One option to segment the laminations that is commonly used for stators is depicted in Fig. 7*b*. The easy magnetisation axis is placed into the yoke to improve the local flux guidance (see Fig. 8). Another possibility is to locate the easy axis in the teeth. The choice between these two options depends on the geometry. The easy axis reduces the magnetic resistance, while the hard axis increases it. Therefore, locating the easy axis in the teeth is recommended as long as the yoke is wider than the teeth. Additionally to the stator segmentation, the rotor is segmented in that fashion that the easy axis shows from one pole to another (see Fig. 8), assuming that the mechanical properties can be fully guaranteed.

In the following, an exemplary machine depicted in Fig. 8 is simulated for the different segmentations previously outlined. The machine has a length of 0.5 m, 90 turns per coil and the phases are star connected. The number of pole pairs is two and the remanence of the magnets is assumed to be 1 T. The yoke has a width of 15 mm. The joints of the segments are idealised and the secondary air gaps neglected for this numerical example, while in reality, more complex joints have to be used [26]. For the investigation of the stator segment orientation, two different cases are considered: in the first case, the stator segments have their easy direction as shown in Fig. 7*b* and in the second the orientation of the easy axis is parallel to the teeth. To evaluate the influence of the anisotropy, the machine is also simulated by an isotropic approach as well as an anisotropic model without segmentation. In all cases, the magnets are mounted onto the rotor laminations and the upper magnet has an outward magnetisation, while the ones on the side have an inward magnetisation.

To use the full capacity of the material's anisotropy, the segmentations of the rotor are assembled in such a way that the easy axes are parallel to the flux in the rotor, indicated by the arrows inside the rotor in Fig. 8. Owing to geometrical symmetry and by using binary boundary conditions, only one half of the machine has to be fully modelled. The simulation cases are as follows: the first case is simulated in a conventional way, assuming isotropic material behaviour.

This approach is used if the machine is fabricated traditionally as in Fig. 6*a*, also including a scalar representation of the material. The scalar isotropic characteristic is achieved by the average of the RD and TD measurements as shown in Fig. 9.

The second case considers the magnetic anisotropy; however, the entire geometry is oriented to the RD horizontally, representing the simultaneous cutting method and no phase shifting of the laminations in the stacking process. The third simulation case takes in Fig. 8 depicted segmentation into account. The easy axis is parallel to the yoke. Finally, the fourth simulation considers the segmented stator with the easy axis located in the teeth.

In Fig. 10, it is shown that the deviation in means of torque is negligibly small. Case one produces the highest torque and the torques of the other cases are <0.1% smaller when compared with the reference. This is because the field in the ferromagnetic parts is different for all cases, but the flux density in the air gap remains almost the same. Since the air gap is the only location, in which the electromagnetic energy conversion takes place, and therefore the torque is not significantly affected [14].

Since the influence of anisotropic material on the field distribution is another aspect of interest, the solution for the first time step is depicted in Fig. 11. It can be perceived that the flux densities in the yoke and the region around the teeth roots are considerably deviating from the isotropic reference simulation, yet the flux density in the air gap is approximately the same. This confirms the consideration stated above regarding the torque. Since different material characteristics exist in each segment due to the phase shift drawn in Fig. 8, the lines of equipotential show a refractive behaviour because of the interface conditions of the field quantities. Comparing the third and the fourth simulations, the shift of the easy axis by 90° in the stator produces a considerable difference in the flux distribution. The equipotential lines in Figs. 11*b*–11*d* clearly show the influence of the anisotropy as described earlier. For case two, the easy direction lies in the *x*-axis and the TD in the *y*-axis. The equipotential lines show the path of the flux density, indicating the easiest path for the flux. For example, the root of the tooth in 120° reveals this with a different shape of the curvature of the equipotential lines. The third case shows the biggest deviation due to the many different directions and material interfaces. The simulations outline that the developed model can accurately simulate complicated segmented geometries built of an anisotropic material.

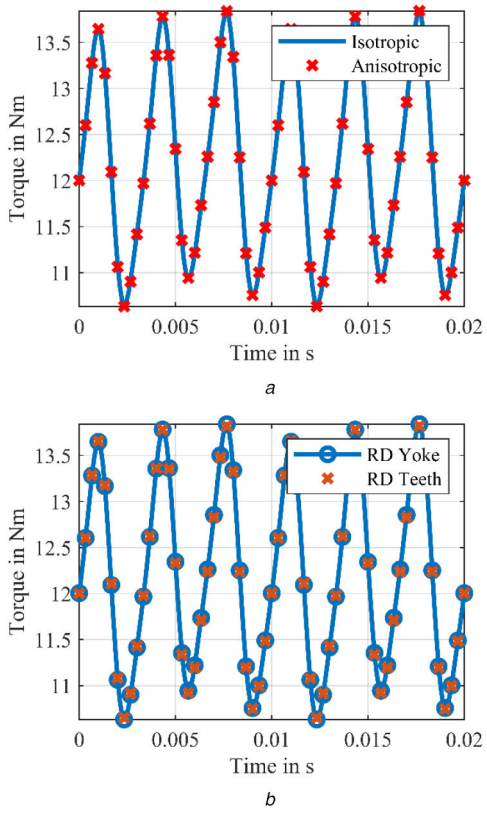

Fig. 10 *Torque for simulation cases*
(a) Unsegmented simulation Case 1 – isotropic material, Case 2 – anisotropic material, ***(b)*** Segmented simulation with anisotropic material Case 3 – easy axis located in the yoke, Case 4 – easy axis placed in the teeth

To further evaluate the influence of the different configurations, the difference (13) between the anisotropic and isotropic approaches is shown in Fig. 12

$$\| \boldsymbol{B}_{\text{iso}} - \boldsymbol{B}_{\text{aniso}} \| \tag{13}$$

It can be depicted that the rotor region is affected by the segmentation as well as the stator. The flux flows closer to the rotor surface and does not penetrate as deep as in the isotropic case. Particularly, the transition from the teeth into the yoke shows a high difference and reaches local deviations of 20% compared with the isotropic simulation.

Furthermore, it can be said that the deviation in the yoke is higher for the third simulation case, while the deviation is bigger in the teeth for case four. The deviation of the flux density inside the teeth might have an influence on the force acting on the teeth. Moreover, it can be depicted that the air gap, as well as the magnets, are barely affected by the anisotropy of the steel sheets. This confirms the conclusion that the torque of the exemplary synchronous machine with surface magnets is not affected significantly, and therefore it is acknowledgeable that the machine torque characteristic persists, while significantly reducing the material waste. In machines with a smaller air gap such as induction machines and reluctance machines, the influence can be stronger [14, 29, 30]. It must be stated that for those machines the impact of secondary air gaps, which occur by the segmentation, has to be considered.

Besides the consideration of the directional dependent material behaviour, the MBMR allows for the simulation of angular shifted vectorial quantities of $\boldsymbol{H}$ and $\boldsymbol{B}$, which can be directly found in the measurements. The phase lag between $\boldsymbol{H}$ and $\boldsymbol{B}$ for the third and fourth cases is depicted in Fig. 13. $\boldsymbol{H}$ and $\boldsymbol{B}$ are located collinearly in the middle of the tooth and it can be recognised that the angular displacement shows a maximum in the root. The phase shift between $\boldsymbol{H}$ and $\boldsymbol{B}$ provides information of the location of the easy axis as well; for case three, $\boldsymbol{H}$ lags behind $\boldsymbol{B}$, while for the fourth case $\boldsymbol{H}$ is in front of $\boldsymbol{B}$. In Fig. 14, the loci for $\boldsymbol{B}$ and $\boldsymbol{H}$ are shown

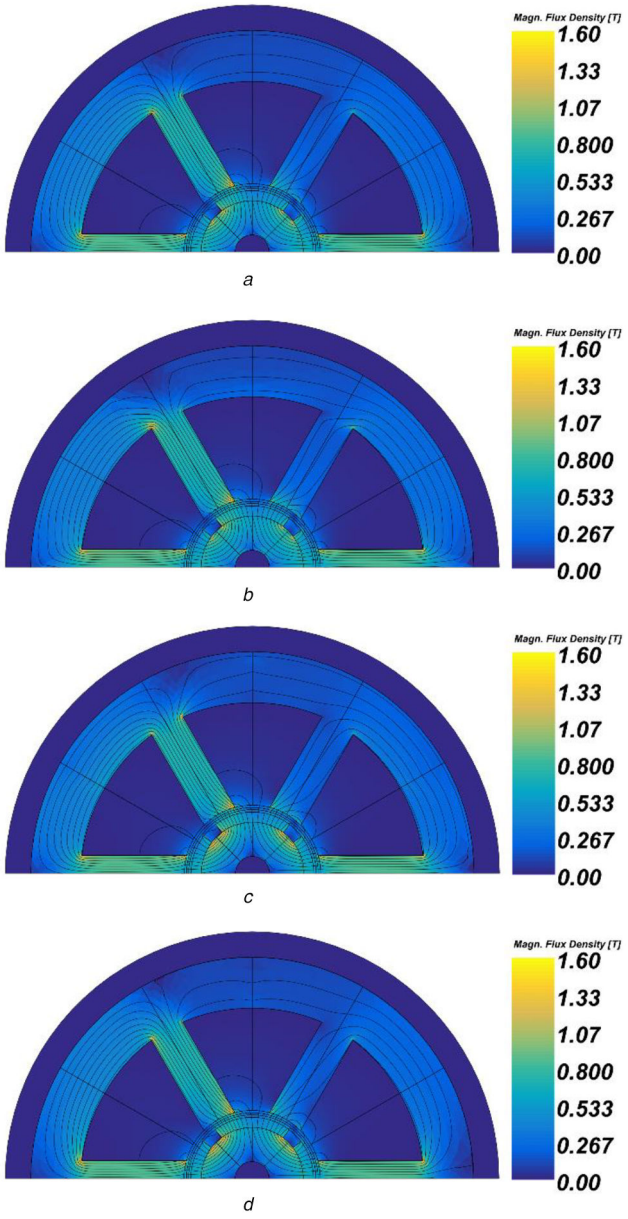

Fig. 11 *Field distribution*
(a) Case 1 – isotropic material, ***(b)*** Case 2 – anisotropic material without segmentation, ***(c)*** Case 3 – segmentation with an easy direction parallel to the yoke, ***(d)*** Case 4 – segmentation with an easy direction parallel to the teeth

for an element in the tooth root. It can be concluded that the isotropic material results in an elliptical locus, while the anisotropic material does not.

The peaks in the $\boldsymbol{H}$-locus in Fig. 14*b* originate from the measured data and can be easily smoothed by measuring in smaller angular steps.

5 Conclusion

The segmentation of electrical machines offers improvements regarding design, automated production and material savings. Owing to the not ideal isotropic behaviour of electrical steel sheets, anisotropy is not indispensable. In this paper, a measurement-based tensorial material representation is introduced and successfully applied to an electrical machine. The measurements contain all information of the direction-dependent magnetisation behaviour of the material, and therefore an algebraic model is no longer needed, in comparison with other anisotropy models. The performed simulations demonstrate the strength of this approach as well as the influence of anisotropy on the simulation results. Although the torque is not notably influenced, the field distribution deviates from the isotropic case, which will have an impact on the local loss

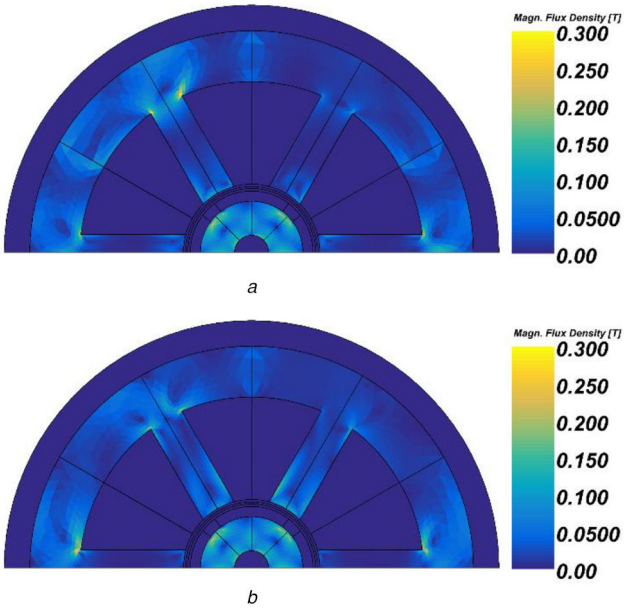

Fig. 12 *Local flux density difference*
(a) Isotropic – Case 3, ***(b)*** Isotropic – Case 4

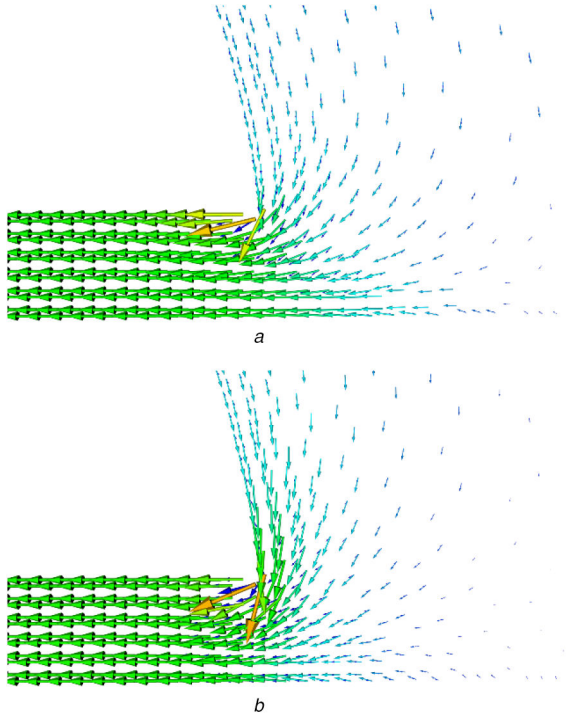

Fig. 13 *Vectorial behaviour of H (dark blue) and B in the tooth for the first time step*
(a) Case 3 easy axis located in the yoke, ***(b)*** Case 4 easy axis located in the teeth

distribution, and therefore on the total losses [31]. To accurately model the anisotropic losses, a vectorial iron loss formula needs to be developed, which can also be based on measurements of the presented RSST. Another approach to represent the iron losses is given by vector hysteresis models. Future work will further investigate the influence on the iron losses as well as the forces acting on the teeth. On the basis of the methodology presented in this paper, an electrical machine with sustainable material utilisation can be designed and accurately simulated taking the vectorial magnetic anisotropy into account.

6 Acknowledgments

This work was supported by the Deutsche Forschungsgemeinschaft (DFG) within the research Project no. 373150943 'Vector hysteresis modelling of ferromagnetic materials' and 255713208 'FOR 1897 – Low-Loss Electrical Steel for Energy – Efficient Electrical Drives'.

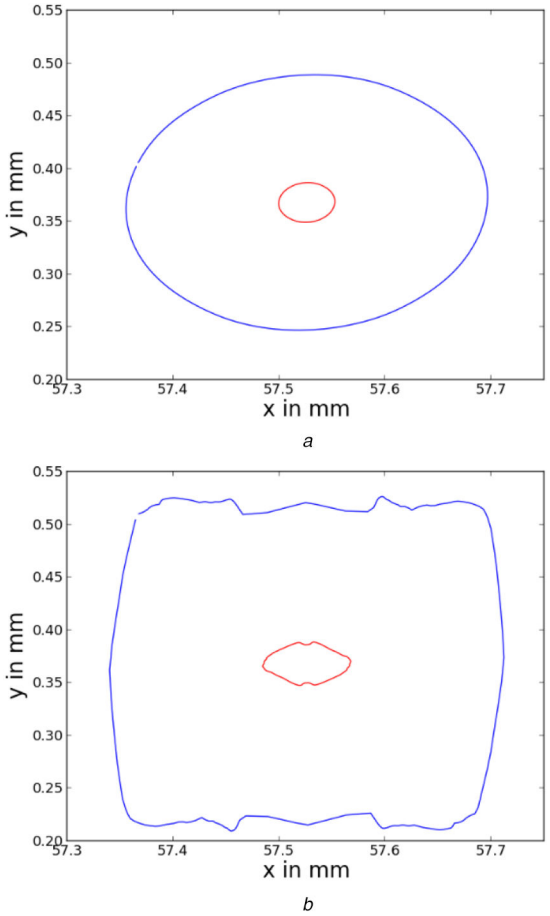

Fig. 14 *B – (red) and **H**-loci (blue) 1 mm is equal to 200 A/m and 9 T*
(a) Isotropic material, ***(b)*** Anisotropic material

7 References

[1] Leuning, N., Steentjes, S., Hameyer, K.: 'On the homogeneity and isotropy of non-grain-oriented electrical steel sheets for the modeling of basic magnetic properties from microstructure and texture', *IEEE Trans. Magn.*, 2017, **53**, (11), pp. 1–5

[2] Littmann, M.F.: 'Iron and silicon–iron alloys', *IEEE Trans. Magn.*, 1971, **7**, (1), pp. 48–60

[3] Leuning, N., Steentjes, S., Heller, M., *et al.*: 'On the correlation of crystallographic macro-texture and magnetic magnetization anisotropy in non-oriented electrical steel', *J. Magn. Magn. Mater.*, 2019, **490**, p. 165485

[4] Landgraf, F.J.G., Yonamine, T., Emura, M., *et al.*: 'Modelling the angular dependence of magnetic properties of a fully processed non-oriented electrical steel', *J. Magn. Magn. Mater.*, 2003, **254-255**, pp. 328–330

[5] Barros, J., Schneider, J., Verbeken, K., *et al.*: 'On the correlation between microstructure and magnetic losses in electrical steel', *J. Magn. Magn. Mater.*, 2008, **320**, pp. 2490–2493

[6] Thabet, A., Abdel-Moamen, M.A., Abdelhady, S.: 'Effective magnetic characterization for new nanocomposites industrial materials using multi-nanoparticles technique'. Proc. 2016 18th Int. Middle East Power Systems Conf. (MEPCON), Cairo, Egypt, 27–29 December 2016, pp. 52–57

[7] Thabet, A., Abdelhady, S., Abdel-Moamen, M.A.: 'Design of multi-nanoparticles technique for enhancing magnetic characterization of power transformers cores', *Adv. Electr. Electron. Eng. J.*, 2018, **16**, (2), pp. 167–177

[8] Cullity, B.D., Graham, C.D.: '*Introduction to magnetic materials*' (IEEE Press, USA, 2009, 2nd edn.)

[9] Thul, A., Steentjes, S., Schauerte, B., *et al.*: 'Rotating magnetizations in electrical machines: measurements and modeling', *AIP Adv.*, 2018, **8**, (5), pp. 1–8

[10] Fiorillo, F., Mayergoyz, I.D.: '*Characterization and measurement of magnetic materials*' (Elsevier Academic Press, USA, 2004)

[11] Bíró, O., Außerhofer, S., Preis, K., *et al.*: 'A modified elliptic model of anisotropy in non-linear magnetic materials', *COMPEL*, 2010, **29**, (6), pp. 1482–1492

[12] Chwastek, K.: 'Anisotropic properties of non-oriented steel sheets', *IET Electr. Power Appl.*, 2013, **7**, (7), pp. 575–579

[13] Xiong, Y.X., Chen, J.Q., Su, Z.Z., *et al.*: 'Numerical computation of static magnetic-field considering 2D property of silicon steel'. Proc. 2015 IEEE Int. Conf. Applied Superconductivity and Electromagnetic Devices (ASEMD), Shanghai, China, November 2015, pp. 345–346

[14] Higuchi, S., Takahashi, Y., Tokumasu, T., *et al.*: 'Comparison between modeling methods of 2D magnetic properties in magnetic-field analysis of synchronous machines', *IEEE Trans. Magn.*, 2014, **50**, (2), pp. 373–376
[15] Urata, S., Enokizono, M., Todaka, T., *et al.*: 'Magnetic characteristic analysis of the motor considering 2D vector magnetic property', *IEEE Trans. Magn.*, 2006, **42**, (6), pp. 615–618
[16] Zeze, S., Todaka, T., Enokizono, M.: 'Vector magnetic characteristic analysis of a surface permanent magnet motor by means of complex E&S modeling', *IEEE Trans. Magn.*, 2012, **48**, (2), pp. 967–970
[17] Bavendiek, G., Leuning, N., Mueller, F., *et al.*: 'Magnetic anisotropy under arbitrary excitation in finite element models', *IEEE Trans. Magn.*, 2009, **45**, (3), pp. 1716–1719
[18] Kameari, A., Fujiwara, K.: 'FEM computation of magnetic fields in anisotropic magnetic materials', *IEEJ Trans. Power Energy*, 2006, **126**, (2), pp. 141–146
[19] Müller, F., Bavendiek, G., Leuning, N., *et al.*: 'Consideration of ferromagnetic anisotropy in electrical machines built of segmented silicon steel sheets'. Proc. Tenth Int. Conf. Computational Electromagnetics, Edinburgh, UK, June 2019, pp. 1–6
[20] Jiles, D.: '*Introduction to magnetism and magnetic materials*' (CRC Press, London, 1991, 3rd edn.)
[21] Börnstein, L.: '*Magnetic properties of metals*', vol. **3** (Springer-Verlag, Berlin, 1986)
[22] Krüttgen, C., Steentjes, S., Glehn, G., *et al.*: 'Parametric homogenized model for inclusion of eddy currents and hysteresis in 2D finite element simulation of electrical machines', *IEEE Trans. Magn.*, 2017, **53**, (6), pp. 1–4
[23] Leite, J.V., Benabou, A., Sadowski, N., *et al.*: 'Finite element three-phase transformer modeling taking into account vector hysteresis model', *IEEE Trans. Magn.*, 2009, **45**, (3), pp. 1716–1719
[24] Hoffman, K., Bastos, J.P.A, Leite, J.V., *et al.*: ' Vector Jiles–Atherton model for improving the FEM convergence', *IEEE Trans. Magn.*, 2017, **53**, (6), pp. 1–4
[25] Bastos, J.P.A., Sadowski, N., Leite, J.V., *et al.*: 'A differential permeability 3D formulation for anisotropic vector hysteresis analysis', *Arch. Electr. Eng.*, 2019, **68**, (2), pp. 455–466
[26] Albrecht, T., Gürsel, C., Lamprecht, E., *et al.*: 'Joining techniques of the rotor segmentation of PM-synchronous machines for hybrid drives'. Proc. 2012 Second Int. Electric Drives Production Conf. (EDPC), Nuremberg, Germany, October 2012, pp. 1–8
[27] El-Refaie, A.N.: 'Fractional slot concentrated-windings synchronous permanent magnet machines: opportunities and challenge', *IEEE Trans. Ind. Electron.*, 2009, **57**, (1), pp. 107–121
[28] Weiss, H.A., Tröber, P., Golle, R., *et al.*: 'Impact of punching parameter variations on magnetic properties of non-grain-oriented electrical steel', *IEEE Trans. Ind. Appl.*, 2018, **54**, (6), pp. 5869–5878
[29] Taghavi, S., Pillay, P.: 'A novel grain-oriented lamination rotor core assembly for a synchronous reluctance traction motor with a reduced torque ripple algorithm', *IEEE Trans. Ind. Appl.*, 2016, **52**, (5), pp. 3729–3738
[30] Herranz Gracia, M., Hameyer, K.: 'Influence of the magnetic anisotropy on electrical machines', in (Eds.): *'Studies in applied electromagnetics and mechanics, advanced computer techniques in applied Electromagnetics'*, vol. **30** (IOS Press, Amsterdam, 2008), pp. 39–46
[31] Pluta, W.: 'Calculating power loss in electrical steel taking into account magnetic anisotropy', *Prz. Elektrotech.*, 2018, **1**, (2), pp. 102–105